

Research Article

Lattice Dynamics and Transport Properties of Multiferroic DyMn_2O_5

Javed Ahmad,¹ Syed Hamad Bukhari,¹ M. Tufiq Jamil,¹ Mehr Khalid Rehmani,¹ Hammad Ahmad,² and Tahir Sultan³

¹Department of Physics, Bahauddin Zakariya University, Multan 60800, Pakistan

²Nanoscience and Technology Department, National Center for Physics, Quaid-i-Azam University Campus, Islamabad 45320, Pakistan

³Department of Civil Engineering, Bahauddin Zakariya University, Multan 60800, Pakistan

Correspondence should be addressed to Javed Ahmad; dr.j.ahmad@gmail.com

Received 12 December 2016; Revised 16 February 2017; Accepted 20 February 2017; Published 7 March 2017

Academic Editor: Mohindar S. Seehra

Copyright © 2017 Javed Ahmad et al. This is an open access article distributed under the Creative Commons Attribution License, which permits unrestricted use, distribution, and reproduction in any medium, provided the original work is properly cited.

We have investigated the optical and electrical properties of polycrystalline DyMn_2O_5 synthesized by sol-gel method. Analysis of the reflectivity spectrum has led to the observation of 18 infrared (IR) active phonon modes out of 36 predicted ones. We discuss the results in terms of different phonon bands originated as a result of atomic vibrations. Moreover, the optical energy band gap of $E_{g(\text{OC})} \sim 1.78$ eV has been estimated from optical conductivity ($\sigma_1(\omega)$) spectrum. The energy band gap and optical transitions were also determined from UV-visible absorption spectrum and band gap of $E_{g(\text{UV})} \sim 1.57$ eV was estimated. Moreover, DC electrical resistivity shows the p-type polaronic conduction above room temperature.

1. Introduction

Manganites RMn_2O_5 , typical type-II multiferroics, usually show large coupling between spin (magnetism), charge (ferroelectricity), and lattice (structure). RMn_2O_5 compounds show cascade of phase transitions with characteristic temperature at Néel transition $T_N = 40\text{--}45$ K and ferroelectric transition at $T_C = 28\text{--}39$ K and ordering of rare-earth moments occurs below 10 K [1]. Until recently, it is well known that RMn_2O_5 crystallize in the orthorhombic structure with $Pbam$ space group at room temperature [2]. However, very recently it is proposed that RMn_2O_5 crystallize in two possible monoclinic space groups Pm and $P2$ depending on the existence of polarization in ab plane and along c axis, respectively [3].

Among the family of RMn_2O_5 , DyMn_2O_5 exhibits remarkable magnetodielectric behavior as compared to other RMn_2O_5 compounds [4]. An unconventional behavior of phonon anomalies in RMn_2O_5 ($R = \text{Bi}, \text{Eu}, \text{Dy}$) has been observed in the paramagnetic phase [5]. They have suggested that these anomalies at new characteristics temperature $T^* \sim 1.5T_N$ are related to the spin-phonon coupling and signaling a transition between states. Moreover, spin-phonon coupling

has been observed slightly above T_N indicating the drastic change in phonon frequency due to magnetic field and temperature [6, 7]. Remarkably, recently we have observed an unconventional magnetodielectric effect in DyMn_2O_5 above T_N , where the infrared and Raman phonons have shown spin-phonon coupling and confirm the strong correlation between spin, charge, and lattice degree of freedom [8]. Such a strong interplay between many degrees of freedom in the paramagnetic phase is a special characteristic of RMn_2O_5 family [5–9]. The knowledge of lattice vibrations and their correlation to different conduction mechanisms is of crucial importance for engineering the materials for various technological applications. However, currently there is no report on the correlation between IR active phonon and the conduction mechanism for DyMn_2O_5 .

In this work, we have measured the IR reflectivity spectrum of DyMn_2O_5 and assign the IR active phonon modes with theoretically calculated modes. In addition, we have performed UV-visible spectroscopy and temperature dependent electrical response to observe the microscopic conduction mechanism. The main objective of this paper is to investigate the lattice vibration in DyMn_2O_5 and the possible correlation

to electronic transport mechanism through energy band gap and activation energy.

2. Experiment

The sample was synthesized by using the sol-gel technique as described previously [9]. Stoichiometric amounts of Gd and Mn nitrates were dissolved into distilled water and stirred for 2 h along with heating at 80°C until viscous gel was formed. The obtained gel was dried at 150°C for 2 h and finally the obtained black powder was sintered at 1000°C for 6 h. Single phase character of prepared sample has been checked by using X-ray diffraction (XRD) pattern. The measurements were performed with the help of Bruker D8 Advance diffractometer with Cu-K α source having wavelength 1.5405 Å. Microstructure was observed by using the scanning electron microscopy (SEM) and image was taken at accelerating voltage of 10 KV and magnification of 80 K. The powder was uniaxially pressed into pellets of 13 mm diameter under the pressure of 30 KN by using the Paul-Otto Weber hydraulic press to obtain high density ceramics for the reflectivity measurement. One of the surfaces of the disc shaped sample was made smooth prior to spectroscopic measurements. Room temperature infrared reflectivity has been measured using Fourier transform infrared spectrometer (Vertex 80v) at near-normal incidence mode. The frequency measurements in the mid-range (550–7500 cm⁻¹) and far (30–680 cm⁻¹) infrared regions were performed using KBR-DLaTGS and Mylar 6 μ m DLaTGS beam splitter-detector combinations, respectively. Mid and far infrared spectra were obtained under vacuum purges, by averaging 100 scans, with spectral resolution of 2 cm⁻¹. A gold mirror was initially used as reference spectrum. The reflectivity spectra in the mid and far infrared regions matched well in the superposition region (550–680 cm⁻¹). The absorption spectra in the 200–1000 nm wavelength region have been obtained using Perkin Elmer Lambda 950 UV/vis/NIR spectrophotometer. The electrical measurements were made by using Keithley source meter 2400, while applying the voltage range of 0–20 V in the temperature range 300–475 K.

3. Results and Discussion

3.1. Structural Analysis. X-ray diffraction (XRD) was performed to check the single phase character of the prepared sample at room temperature and the obtained XRD pattern of DyMn₂O₅ is shown in Figure 1. JANA2006 program was used for the Rietveld refinement of the XRD pattern assuming orthorhombic structure with *Pbam* space group (Figure 2). All the XRD peaks were well fitted confirming the single phase formation and no trace of any impurity peak was found. The obtained unit cell parameters are $a = 7.251$ Å, $b = 8.445$ Å, and $c = 5.647$ Å, which are in good agreement with theoretically calculated values (7.270, 8.518, and 5.600 Å, resp.) as well as experimentally observed values (7.285, 8.487, and 5.668 Å, resp.) [10].

In addition, we have also calculated the strain present in the material and crystallite size by using the Williamson-Hall (W-H) model considering the uniform isotropic crystal for

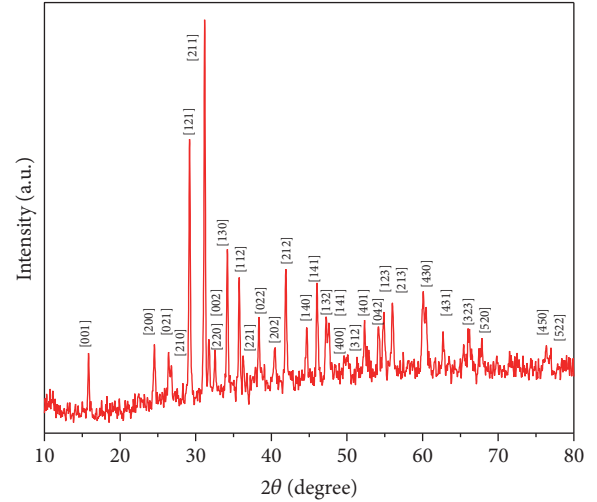


FIGURE 1: Room temperature XRD pattern of DyMn₂O₅.

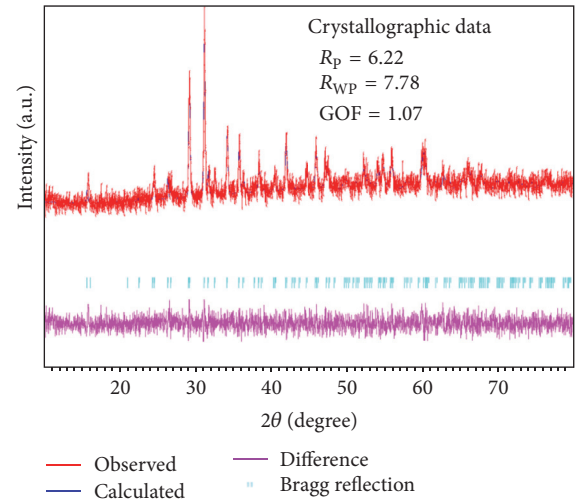


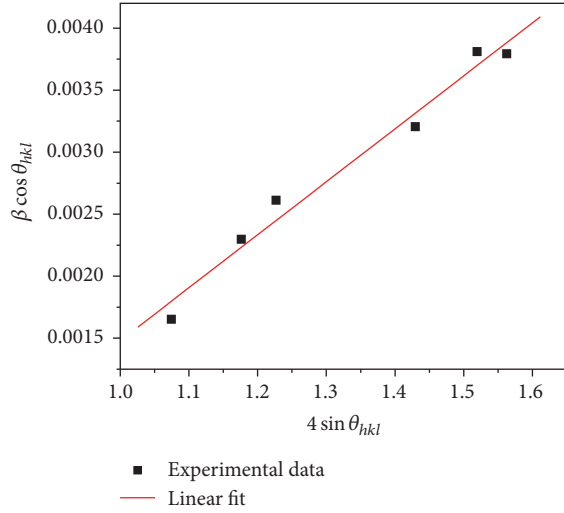
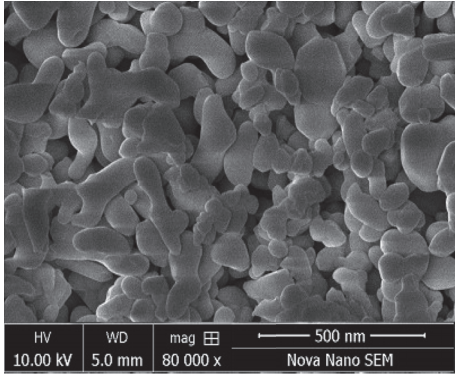
FIGURE 2: Rietveld refinement of XRD pattern where solid (red line) is the observed data and solid curve (blue line) is the best fit, vertical marks indicate the Bragg peaks, and the bottom curve shows the difference between observed and calculated intensities.

the total peak broadening using the relation [11]

$$\beta_{hkl} \cos \theta_{hkl} = \frac{K\lambda}{D_v} = 4\epsilon \sin \theta_{hkl}, \quad (1)$$

where D_v is the crystallite size, K is the shape factor ($K = 0.9$), λ is the wavelength of X-rays, and $4\epsilon \sin \theta_{hkl}$ is the strain induced line broadening. It is easy to calculate the strain and crystallite size by extracting the slope and the intercept of the linear fit as shown in Figure 3. The obtained values of strain and crystallite size are 4.27×10^{-3} and 50 nm, respectively.

Figure 4 shows the SEM micrograph of DyMn₂O₅. Large grains with less grain boundaries can be clearly seen from micrograph. However, grains show no perfect alignment, which is a typical characteristic of polycrystalline sample. The individual grains shown are of the round shape with an

FIGURE 3: W-H plot of polycrystalline DyMn₂O₅.FIGURE 4: SEM image of DyMn₂O₅ synthesized by sol-gel method.

average grain size ~ 40 nm, which is consistent with crystallite size of ~ 38 nm obtained from XRD analysis by using the well-known Debye-Scherrer formula.

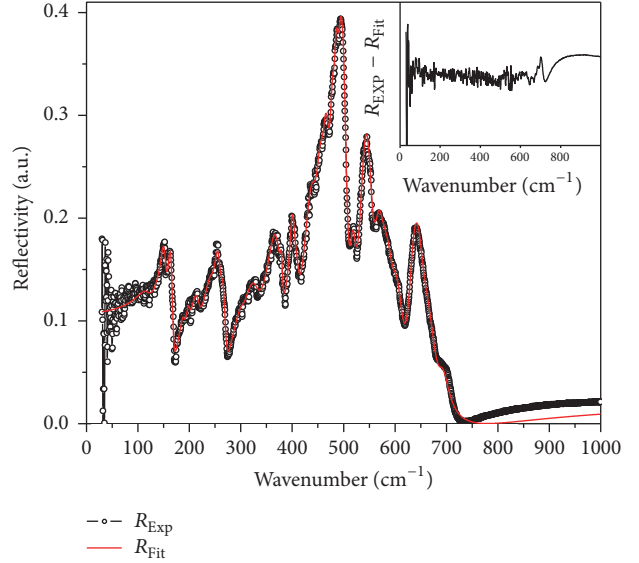
3.2. Infrared Reflectivity. Figure 5 shows the near-normal reflectivity of DyMn₂O₅ in frequency range $30\text{--}1000\text{ cm}^{-1}$ at room temperature. Considering the quasi-normal incidence angle, the optical reflectivity spectrum (R) is related to the dielectric function by Fresnel's formula

$$R(\omega) = \left| \frac{\sqrt{\epsilon(\omega)} - 1}{\sqrt{\epsilon(\omega)} + 1} \right|^2. \quad (2)$$

To quantify the infrared phonon contribution to the dielectric function $\epsilon(\omega)$ is defined as

$$\epsilon(\omega) = \epsilon_{\infty} + \sum_j \frac{\omega_{TO,j}^2 S_j}{\omega_{TO,j}^2 - \omega^2 - i\omega\gamma_j}, \quad (3)$$

where ϵ_{∞} is the high frequency dielectric constant indicating the contribution to the electronic polarization. $\omega_{TO(j)}$, S_j , and γ_j are the optical phonon frequency, oscillator strength, and

FIGURE 5: Infrared reflectivity spectra of DyMn₂O₅ measured at room temperature. The black circles and red line show the experimental data and fitting curve by Lorentz oscillator model, respectively. The inset shows the deviation between measured (R_{EXP}) and fitted (R_{FIT}) reflectivity.

and damping factor of j th phonon, respectively. Both (2) and (3) together can give the measured reflectivity spectrum. Following above relations, the well-known Lyddane-Sachs-Teller (LST) relation becomes as $\epsilon_{\infty}/\epsilon_0 = \omega_{LO}^2/\omega_{TO}^2$, used to calculate the longitudinal optical phonon modes (ω_{LO}).

According to group theoretical analysis, there are 36 infrared active vibrational phonon modes in the paraelectric phase of RMn₂O₅ at the Γ point ($8B_{1u} + 14B_{2u} + 14B_{3u}$) [7, 12]. These modes are classified into different phonon bands which correspond to relative motion of rare-earth, manganese, and oxygen ions. The observed phonon frequencies obtained from the fit are assigned via comparison with those found in lattice dynamics calculations (Table 1) and are in agreement with reported data [7, 12]. Among the 36 theoretically predicted infrared active modes, we are able to observe only 18 modes. The origin of this discrepancy will be discussed later.

As far as the microscopic motion of the active phonon modes is concerned, the phonon modes at 151, 167, 194, 217, and 251 cm^{-1} involve the relative motion of Dy ions with respect to manganese ions of MnO₅ and MnO₆ polyhedra and assigned to the calculated modes between 95 and 245 cm^{-1} , respectively, as can be seen in Figures 6(a)–6(d). Moreover, high frequency modes between 260 and 684 cm^{-1} are attributed to Mn-O bending and stretching motion of the distorted octahedra and square pyramidal building block units. These modes may correspond to the calculated modes between 283 and 728 cm^{-1} and mainly arise from the Mn-O stretching motion within the equatorial plan of the MnO₆ octahedra and Mn-O stretching motion in the axial direction of MnO₅ square pyramids as shown in Figures 6(e)–6(i) [12]. Similar stretching and bending vibration of oxygen atoms at

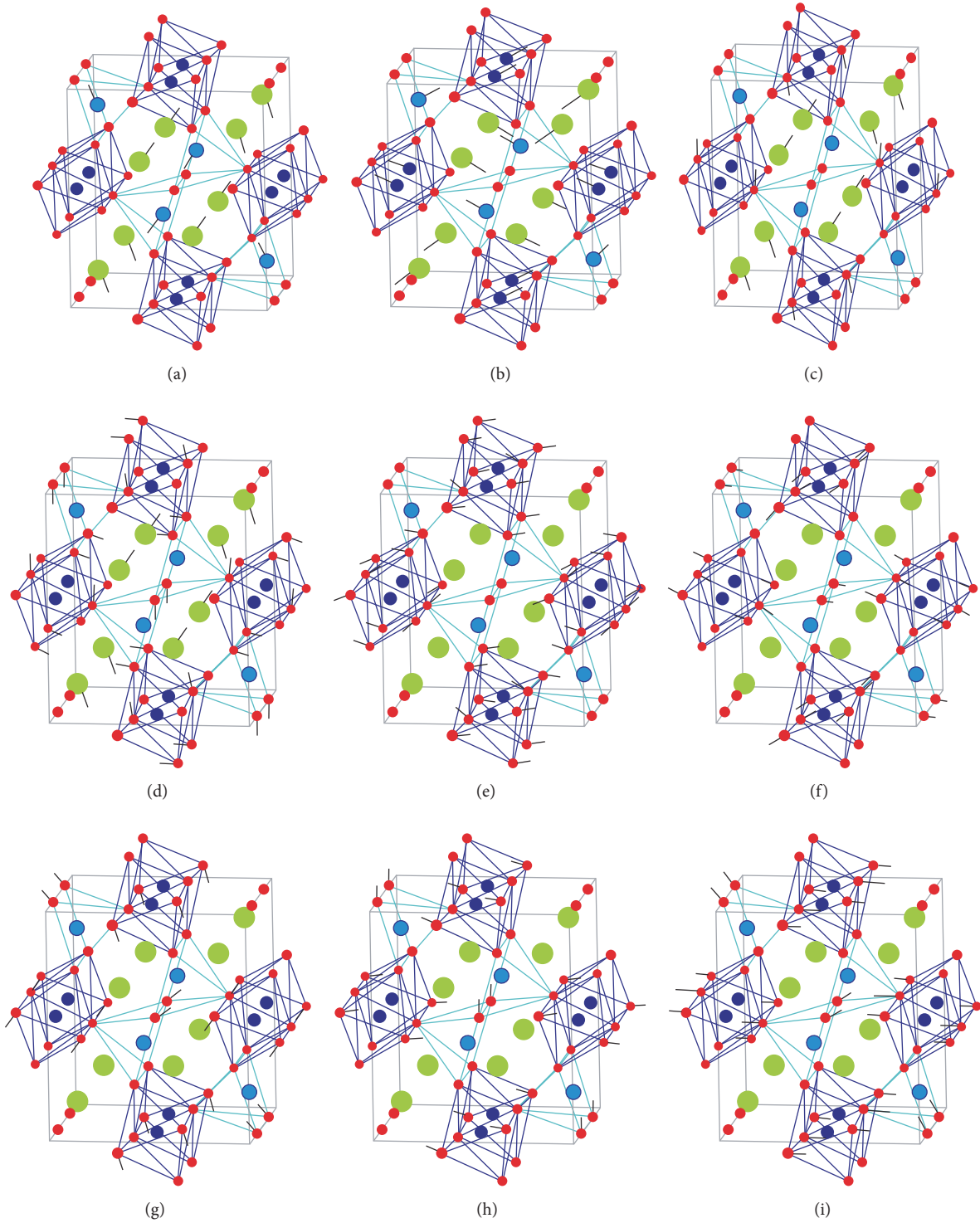


FIGURE 6: Panels (a), (b), (c), (d), (e), (f), (g), (h), and (i) are the representative mode displacement obtained from lattice dynamics calculation [7] with calculated frequencies at 170, 176, 208, 231, 283, 567, 576, 626, and 728 cm^{-1} , respectively.

$>300 \text{ cm}^{-1}$ has also been observed through Raman spectra in RMn_2O_5 ($R = \text{Bi, Tb, Eu, Dy, Ho}$) [5, 13].

As mentioned previously, out of 36 theoretically predicted modes, we have only observed 18 modes. The origin of this discrepancy is due to the polycrystalline nature of our

sample which has mixed ab -plane and c axis response. For example, let us consider the infrared modes of 14B_{2u} and 14B_{3u} that occur in close pair such that at least 10 of them have wavenumber difference less than 10 cm^{-1} , which is due to the typical damping value. This clearly reflects that they

TABLE 1: Phonon-fit parameters of the infrared reflectivity spectrum of DyMn_2O_5 at room temperature and calculated modes [6] for comparison. The wavenumbers $\omega_{\text{TO(LO)}}$ are given in cm^{-1} . 18 observed modes: $\epsilon_\infty = 2.78$, $\epsilon_s = 5$.

$\omega_{\text{TO(LO)}}$	S_j	γ_j	B_{3u}	B_{2u}	B_{1u}	Assignment
151(204)	0.20	9.29	95	104	117	Relative motion of Mn polyhedra and Dy ions
167(226)	0.28	8.51	170	176	—	
194(262)	0.11	15.4	189	184	—	
217(294)	0.02	4.46	208	—	—	Relative motion of Dy ions and oxygens
251(341)	0.05	4.73	—	231	245	
260(352)	0.22	18.3	—	283	—	Mn-O bending motions in MnO_6 octahedra
291(395)	0.01	10.8	310	—	—	
327(443)	0.05	9.7	336	339	325	Mn-O twisting motions in Mn polyhedra
371(503)	0.27	27.3	382	387	368	
402(544)	0.10	12.72	403	—	—	
433(586)	0.12	27.46	—	441	456	
462(626)	0.10	18.08	475	464	473	Mn-O bending motions within equatorial MnO_2 planes in MnO_6 octahedra
484(655)	0.20	18.25	486	475	—	
511(692)	0.01	7.15	—	—	509	
534(723)	0.16	17.31	567	576	—	Mn-O stretching motions in MnO_6 octahedra and MnO_5 square pyramids
565(765)	0.23	36.58	585	589	—	
628(850)	0.08	23.22	617	626	655	
684(926)	0.02	32.57	762	728	—	

can not be resolved separately by using unpolarized light in polycrystal and that they have been considered together in the fitting procedure.

For quantitative analysis of phonon contribution to the infrared spectrum of DyMn_2O_5 , we have calculated real part of optical conductivity $\sigma_1(\omega) = \omega\epsilon_2/4\pi$ spectrum by using Kramers-Krönig transformation, as shown in Figure 7. $\sigma_1(0)$ is zero suggesting no contribution from free carriers at low frequency range and suggesting the charge carriers are rather localized. Moreover, the optical energy band gap has been calculated from the spectrum of optical conductivity [see inset of Figure 7]. An optical band gap can be observed as a gradual onset of the spectral intensity showing a sharp rise, as determined by the crossing point of the energy axis [14, 15]. The band gap distinctly seen at $E_{g(\text{OC})} \sim 1.78$ eV arises due to lowest energy oscillator, close to the band gap (~ 1.70 eV) observed for TbMn_2O_5 through ellipsometry technique [16].

3.3. UV-Visible Spectroscopy. We have measured UV-visible absorption spectrum of DyMn_2O_5 in the wavelength range 200–1000 nm as shown in Figure 8. The diffuse reflectance spectrum has been transformed into Kubelka-Munk function or absorption ($F(R)$) by using the Kubelka-Munk theory [17, 18]. Such strong absorption with cutoff wavelength at 1000 nm indicates that DyMn_2O_5 can efficiently absorb light over a broad range of wavelengths including the complete visible range (390–780 nm). Moreover, we have observed two strong absorption peaks at about 485 nm and 525 nm which reflects that there is a probability of e_g electrons from Mn^{3+}

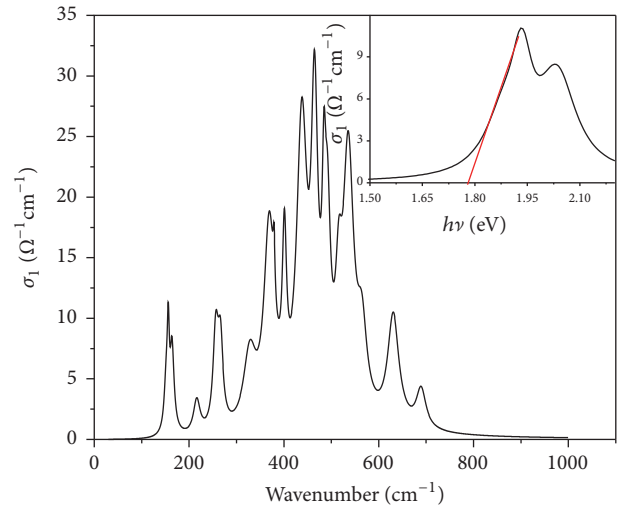


FIGURE 7: Real part of optical conductivity of DyMn_2O_5 at room temperature. Inset shows the estimated energy band gap, where the linear portion of the lowest energy extrapolated to the energy axis to obtain the energy band gap (~ 1.78 eV).

($t_{2g}^3 e_g^1$) ions tunnel to Mn^{4+} ($t_{2g}^3 e_g^0$) ions, giving rise to the local distortion near these ions [19]. These strong absorption peaks may be attributed to the $3d$ -electronic transitions of $\text{Mn}^{3+}/\text{Mn}^{4+}$.

In order to verify the energy band gap estimated from optical conductivity, we have calculated the energy band gap

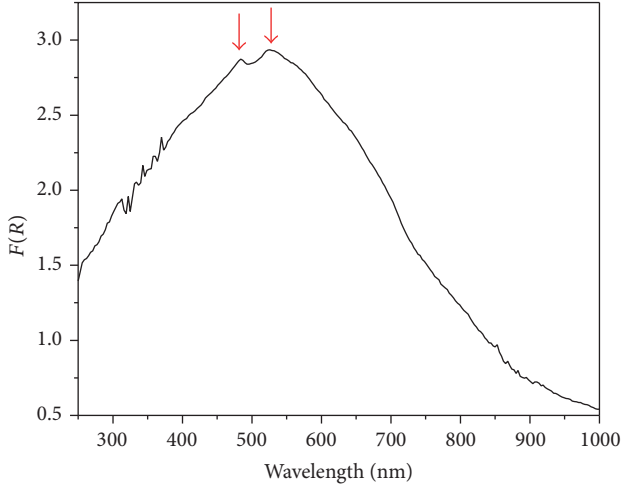


FIGURE 8: Kubelka-Munk function versus wavelength for DyMn_2O_5 .

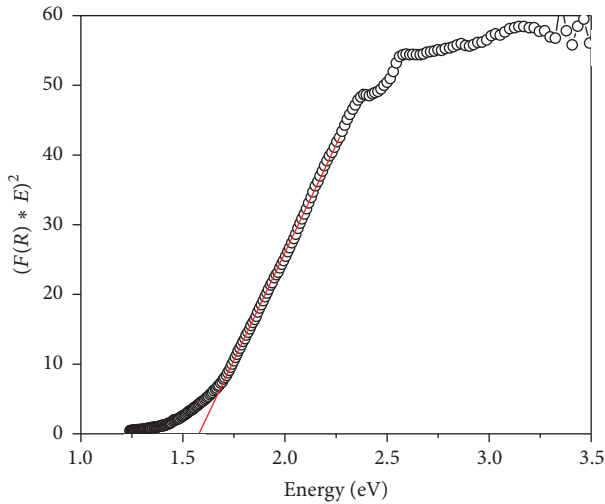


FIGURE 9: Determination of band gap from the inflection point of the $(F(R) * E)^2$ versus E .

by using the relation [20]

$$(F(R)hv)^n = A(hv - E_g), \quad (4)$$

where hv is the energy of the incident photon, $F(R)$ is the K-M function, A is a characteristic parameter, and E_g is the band gap. Exponent n specifies the type of transition and it may be $1/2$ or 2 for the direct forbidden or indirect transition, respectively. Here, we have estimated the indirect band gap from the plot of $(F(R)hv)^2$ versus energy ($E = hv$) by extrapolating the linear portion to the energy axis (i.e., $F(R) = 0$) to determine the energy band gap of about $E_{g(\text{UV})} \sim 1.57$ eV as shown in Figure 9. We have observed a comparable energy band gap estimated through optical conductivity ($E_{g(\text{OC})} \sim 1.78$ eV) and UV-visible ($E_{g(\text{UV})} \sim 1.57$ eV). Despite the slight difference in energy band gap ($\Delta = 0.21$ eV), DyMn_2O_5 exhibits a semiconducting behavior. The obtained value of band gap is close to the band gap

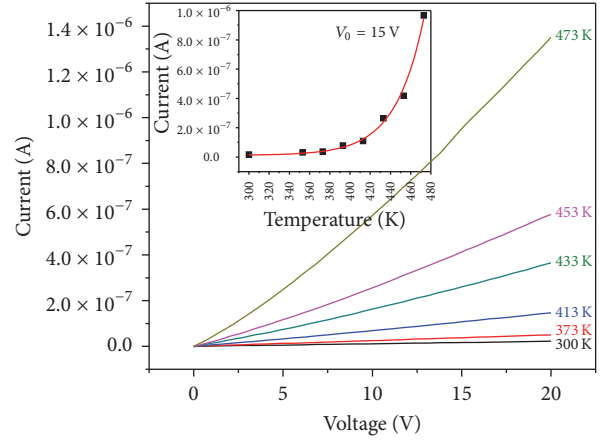


FIGURE 10: I - V characteristics of DyMn_2O_5 at different temperatures. Inset shows variation of current with temperature.

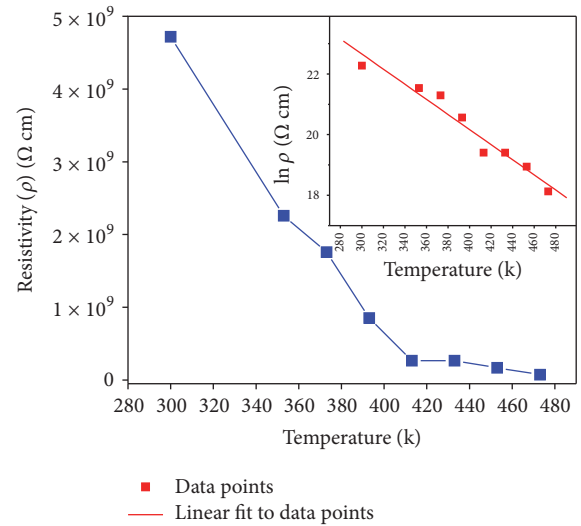


FIGURE 11: Variation of resistivity with temperature of DyMn_2O_5 . Inset shows logarithmic variation of resistivity with temperature.

observed for similar compounds such as $\text{TbMn}_2\text{O}_5 \sim 1.70$ eV, $\text{YMn}_2\text{O}_5 \sim 1.21$ eV [16, 21].

3.4. Electrical Properties. In order to study the conduction mechanism, we have performed temperature dependent I - V characteristics of DyMn_2O_5 which demonstrate a smooth increase in current with increase in applied voltage (0–20 V) as shown in Figure 10. Moreover, at a certain voltage (i.e., $V_0 = 15$ V) current increases with increase in temperature supporting a semiconducting nature of the material [see inset of Figure 10]. Temperature dependent DC electrical resistivity of DyMn_2O_5 system has been measured in the temperature range (300–473 K), as shown in Figure 11. The logarithmic variation of resistivity with temperature is also shown [see inset of Figure 11]. It follows the Arrhenius rule with positive slope as shown in Figure 12. The plot in Figure 12

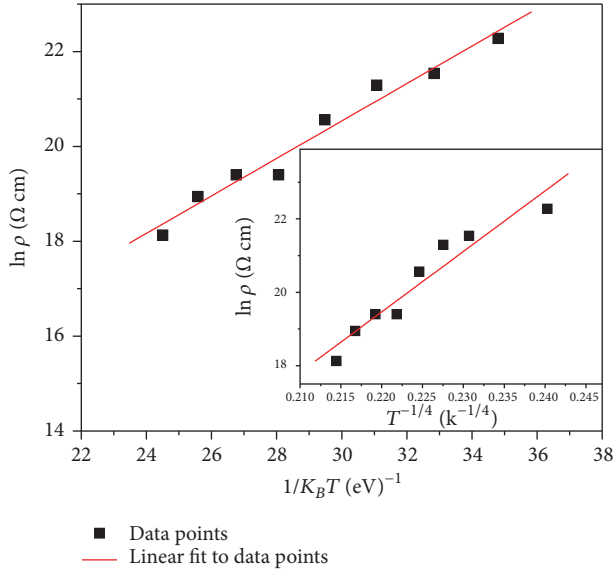


FIGURE 12: Arrhenius plot of DyMn_2O_5 . Inset shows logarithmic variation of resistivity versus $T^{-1/4}$.

is extracted from the given equation

$$\rho = \rho_0 \exp\left(\frac{-\Delta E}{K_B T}\right), \quad (5)$$

where ΔE is activation energy, T is absolute temperature, and K_B is Boltzmann constant.

The activation energy ~ 0.759 eV for DyMn_2O_5 is calculated from slope of $\ln \rho$ versus $1/K_B T$. This may be explained in terms of dominant character of grain boundaries to find out the resistive properties of this system. Generally, activation energies for the oxide ionic conductors are >0.9 eV. It is usually <0.2 eV for n-type polaronic conduction of electrons and >0.2 eV for the polaronic conduction of holes [22]. In our case, observed value of activation energy suggests a p-type polaronic conduction of holes above room temperature in DyMn_2O_5 . Moreover, the temperature dependent DC resistivity (see Figure 11) shows decrease in resistivity with the increase in temperature reflecting the role of thermally activated charge carriers according to the hopping conduction mechanism [23–25]. We have tested the validity of this polaronic hopping conduction mechanism in the same temperature range (300–473 K) by Mott's variable-range-hopping (VRH) conduction rule [26–28]

$$\rho = \rho_0 \exp\left(\frac{T_0}{T}\right)^{1/4}. \quad (6)$$

It is observed that variation of $\ln \rho$ with $T^{-1/4}$ is a straight line as depicted in inset of Figure 12. The linear dependence in our case confirms the presence of hopping type conduction in given temperature range [29–31]. Moreover, the obtained value of ΔE is almost equal to half of the optical energy band gap (1.78 eV), confirming the correlation between thermally activated charge carriers with localized free-carrier response. The obtained value of activation energy (0.759 eV)

of DyMn_2O_5 in our investigated compound is comparable with Mn based compound such as SmMn_2O_5 for which activation energy is 0.59 eV [32].

4. Conclusion

We have investigated the infrared reflectivity, UV-visible absorption spectra, and electrical conduction mechanism of polycrystalline DyMn_2O_5 . The experimentally observed phonon modes have been assigned to the different lattice dynamics and crystal symmetry. In addition, we have calculated optical conductivity, and no contribution of free carriers has been observed at low frequency. On comparison, an agreement found between energy band gap estimated through UV-visible measurement and optical conductivity and is associated with the semiconducting behavior of DyMn_2O_5 . Indeed, the semiconducting mechanism has also been confirmed from existence of p-type polaronic conduction above room temperature. The results conclude DyMn_2O_5 as a typical semiconductor.

Conflicts of Interest

The authors declare that there are no conflicts of interest regarding the publication of this paper.

References

- [1] M. Tachibana, K. Akiyama, H. Kawaji, and T. Atake, "Lattice effects in multiferroic $R\text{Mn}_2\text{O}_5$ ($R = \text{Sm} - \text{Dy}, \text{Y}$)," *Physical Review B—Condensed Matter and Materials Physics*, vol. 72, no. 22, Article ID 224425, 2005.
- [2] P. G. Radaelli and L. C. Chapon, "A neutron diffraction study of RMn_2O_5 multiferroics," *Journal of Physics Condensed Matter*, vol. 20, no. 43, Article ID 434213, 2008.
- [3] V. Balédent, S. Chattopadhyay, P. Fertey et al., "Evidence for room temperature electric polarization in RMn_2O_5 multiferroics," *Physical Review Letters*, vol. 114, no. 11, Article ID 117601, 2015.
- [4] N. Hur, S. Park, P. A. Sharma, S. Guha, and S.-W. Cheong, "Colossal magnetodielectric effects in DyMn_2O_5 ," *Physical Review Letters*, vol. 93, no. 10, Article ID 107207, 2004.
- [5] A. F. García-Flores, E. Granado, H. Martinho et al., "Anomalous phonon shifts in the paramagnetic phase of multiferroic RMn_2O_5 ($R = \text{Bi}, \text{Eu}, \text{Dy}$): possible manifestations of unconventional magnetic correlations," *Physical Review B - Condensed Matter and Materials Physics*, vol. 73, no. 10, Article ID 104411, 2006.
- [6] J. Cao, L. I. Vergara, J. L. Musfeldt et al., "Spin-lattice interactions mediated by magnetic field," *Physical Review Letters*, vol. 100, no. 17, Article ID 177205, 2008.
- [7] J. Cao, L. I. Vergara, J. L. Musfeldt et al., "Magnetoelastic coupling in DyMn_2O_5 via infrared spectroscopy," *Physical Review B*, vol. 78, no. 6, Article ID 064307, 2008.
- [8] S. H. Bukhari and J. Ahmad, "Evidence for magnetic correlation in the paramagnetic phase of DyMn_2O_5 ," *Physica B: Condensed Matter*, vol. 503, pp. 179–182, 2016.
- [9] S. H. Bukhari and J. Ahmad, "Emergent excitation in the paramagnetic phase of geometrically frustrated GdMn_2O_5 ," *Physica B: Condensed Matter*, vol. 492, pp. 39–44, 2016.

- [10] G. R. Blake, L. C. Chapon, P. G. Radaelli et al., "Spin structure and magnetic frustration in multiferroic RMn₂O₅ (R=Tb,Ho,Dy)," *Physical Review B*, vol. 71, no. 21, Article ID 214402, 2005.
- [11] K. Venkateswarlu, A. Chandra Bose, and N. Rameshbabu, "X-ray peak broadening studies of nanocrystalline hydroxyapatite by Williamson-Hall analysis," *Physica B: Condensed Matter*, vol. 405, no. 20, pp. 4256–4261, 2010.
- [12] R. Valdés Aguilar, A. B. Sushkov, S. Park, S.-W. Cheong, and H. D. Drew, "Infrared phonon signatures of multiferroicity in TbMn₂O₅," *Physical Review B*, vol. 74, no. 18, Article ID 184404, 2006.
- [13] B. Mihailova, M. M. Gospodinov, B. Güttler, F. Yen, A. P. Litvinchuk, and M. N. Iliev, "Temperature-dependent Raman spectra of Ho Mn₂O₅ and TbMn₂O₅," *Physical Review B - Condensed Matter and Materials Physics*, vol. 71, no. 17, Article ID 172301, 2005.
- [14] K. P. Ong, P. Blaha, and P. Wu, "Origin of the light green color and electronic ground state of La Cr O₃," *Physical Review B—Condensed Matter and Materials Physics*, vol. 77, no. 7, Article ID 073102, 2008.
- [15] T. Arima, Y. Tokura, and J. B. Torrance, "Variation of optical gaps in perovskite-type 3d transition-metal oxides," *Physical Review B*, vol. 48, no. 23, pp. 17006–17009, 1993.
- [16] A. S. Moskvina and R. V. Pisarev, "Charge-transfer transitions in mixed-valent multiferroic TbMn₂O₅," *Physical Review B*, vol. 77, no. 6, Article ID 060102, 2008.
- [17] P. Kubelka, "New contributions to the optics of intensely light-scattering materials. I," *Journal of the Optical Society of America*, vol. 38, no. 5, pp. 448–457, 1948.
- [18] S. Thota, J. H. Shim, and M. S. Seehra, "Size-dependent shifts of the Néel temperature and optical band-gap in NiO nanoparticles," *Journal of Applied Physics*, vol. 114, no. 21, Article ID 214307, 2013.
- [19] B. K. Khannanov, V. A. Sanina, E. I. Golovenchits, and M. P. Scheglov, "Room-temperature electric polarization induced by phase separation in multiferroic GdMn₂O₅," *JETP Letters*, vol. 103, no. 4, pp. 248–253, 2016.
- [20] V. Sasca and A. Popa, "Band-gap energy of heteropoly compounds containing keggung polyanion-[PV_xMo₁₂xO₄₀]_i(3+x) relates to counter-cations and temperature studied by uv-vis diffuse reflectance spectroscopy," *Journal of Applied Physics*, vol. 114, no. 13, pp. 133503–133510, 2013.
- [21] H. Yang, S. F. Wang, T. Xian, Z. Q. Wei, and W. J. Feng, "Fabrication and photocatalytic activity of YMn₂O₅ nanoparticles," *Materials Letters*, vol. 65, no. 5, pp. 884–886, 2011.
- [22] M. Idrees, M. Nadeem, and M. M. Hassan, "Investigation of conduction and relaxation phenomena in LaFe 0.9Ni_{0.1}O₃ by impedance spectroscopy," *Journal of Physics D: Applied Physics*, vol. 43, no. 15, Article ID 155401, 2010.
- [23] D. R. Patil and B. K. Chougule, "Effect of resistivity on magnetoelectric effect in (x)NiFe₂O₄-(1-x)Ba_{0.9}Sr_{0.1}TiO₃ ME composites," *Journal of Alloys and Compounds*, vol. 470, no. 1-2, pp. 531–535, 2009.
- [24] J. Ryu, S. Priya, K. Uchino, and H.-E. Kim, "Magnetoelectric effect in composites of magnetostrictive and piezoelectric materials," *Journal of Electroceramics*, vol. 8, no. 2, pp. 107–119, 2002.
- [25] C. M. Kanamadi, G. Seeta Rama Raju, H. K. Yang, B. C. Choi, and J. H. Jeong, "Conduction mechanism and magnetic properties of (x)Ni_{0.8}Cu_{0.2}Fe₂O₄ + (1-x)Ba_{0.8}Pb_{0.2}Ti_{0.8}Zr_{0.2}O₃ multiferroics," *Journal of Alloys and Compounds*, vol. 479, no. 1-2, pp. 807–811, 2009.
- [26] J. M. D. Coey, M. Viret, L. Ranno, and K. Ounadjela, "Electron localization in mixed-valence manganites," *Physical Review Letters*, vol. 75, no. 21, pp. 3910–3913, 1995.
- [27] J. M. De Teresa, M. R. Ibarra, J. Blasco et al., "Spontaneous behavior and magnetic field and pressure effects on La_{2/3}Ca_{1/3}MnO₃ perovskite," *Physical Review B*, vol. 54, no. 2, pp. 1187–1193, 1996.
- [28] M. Viret, L. Ranno, and J. M. D. Coey, "Magnetic localization in mixed-valence manganites," *Physical Review B - Condensed Matter and Materials Physics*, vol. 55, no. 13, 1997.
- [29] M. F. Wasfiq, M. Y. Nadeem, K. Mahmood, M. F. Warsi, and M. A. Khan, "Impact of metal electrode on charge transport behavior of metal-Gd₂O₃ systems," *Journal of Alloys and Compounds*, vol. 648, pp. 577–580, 2015.
- [30] W.-H. Jung, "Evaluation of Mott's parameters for hopping conduction in La_{0.67}Ca_{0.33}MnO₃ above T_c," *Journal of Materials Science Letters*, vol. 17, no. 15, pp. 1317–1319, 1998.
- [31] M. Ziese and C. Srinithiwarawong, "Polaronic effects on the resistivity of manganite thin films," *Physical Review B - Condensed Matter and Materials Physics*, vol. 58, no. 17, pp. 11519–11525, 1998.
- [32] K. Saravana Kumar, N. Aparnadevi, A. Muthukumaran, and C. Venkateswaran, "Phase Stabilization of Fe Substituted SmMn₂O₅: SmFeMnO₅," *Transactions of the Indian Institute of Metals*, vol. 68, no. 5, pp. 693–698, 2015.



Hindawi

Submit your manuscripts at
<https://www.hindawi.com>

